HiSST: 3rd International Conference on
High-Speed Vehicle Science Technology
14 -19 April 2024, Busan, Korea

Some Recent Developments in Hypersonic Flow Stability Analyses

Liang Wang[1], *Song Fu*[2]

Abstract

This paper presents the authors' advancements in the investigation of flow instabilities encountered during hypersonic flight. It encapsulates several significant findings, as follows: 1) Elucidation of the excitation mechanisms governing the evolution of the three-dimensional boundary layer at the vehicle nose, with particular emphasis on the impact of thermal–chemical nonequilibrium effects. 2) Observation of a notable decay in disturbance growth-rate oscillation downstream of the turning point, where the unstable supersonic mode transitions back to the subsonic regime. 3) Discovery of novel modes of crossflow vortices occurring on the surface of swept wings.

Keywords: *Hypersonics, Stability analyses, High Enthalpy Flow, Swept Leading Edge Flow, Concave Surface*

Nomenclature

TCNE – Thermal–Chemical Nonequilibrium
CPG – Calorically Perfect Gas
LST – Linear stability theory
PSE – Linearized Navier-Stokes
DNS – Direct numerical simulation
Ma – Mach number
Re – Reynolds number
T – Temperature
Pr – Prandtl number
γ – Specific heat ratio

1. Introduction

Hypersonic technology stands as a disruptive force shaping the future landscape of warfare and representing a new pinnacle in aerospace technology. Presently, the advancement of near space vehicle approaching hypersonic regimes has extended to broader airspace and higher Mach numbers, undertaking trans-atmospheric flights-ranging from regions of elevated density continuum flow to sparse flow regions to nearly vacuum free-molecular flow areas, each with vastly differing thermodynamic properties. Coupled with high Mach numbers and low environmental pressure/density characteristics, these flow fields exhibit pronounced thermochemical non-equilibrium effects [1], significantly increasing the predictive challenges concerning aerodynamic thermal environments of near space vehicles and the thermal response of ablative materials: on one hand, under high temperature, the excitation of gas particle vibrational energy/electron energy and chemical reaction absorption of substantial energy diminishes flow field temperature, thereby alleviating aerodynamic heating; on the other hand, within the thin boundary layer near the vehicle's surface, a series of composite reactions occur between surface materials and gas atoms, ions, leading to phenomena such as surface oxidation, catalysis, and ablation, releasing significant heat and altering gas composition and energy distribution near the surface. Additionally, thermochemical non-equilibrium effects, wall material ablation/pyrolysis/micro-ablation/oxidation products, cause changes in parameters such as shockwave position and shape, separation zone size, thus affecting the aerothermal loads on the vehicle [2].

Of greater concern, when trans-atmospheric vehicles swiftly entre into lower airspace (between altitudes of 40 to 60 kilometers), air density is considerably higher compared to the upper atmosphere (corresponding to much higher Reynolds numbers), inevitably leading to laminar-to-turbulent transition.

[1] *Tsinghua University, Peking, China, wangliang12@tsinghua.edu.cn*
[2] *Tsinghua University, Peking, China, fs-dem@tsinghua.edu.cn*

Thermal flux on the vehicle's surface grows 3 to 5 times more within the transition region compared to laminar states. Multiple hypersonic flight accidents have been attributed to flow transition. For instance, the tragic incident involving the US Columbia Shuttle: the impact of debris from a detached fuel tank striking the left wing's thermal protection panel caused a local protrusion, leading to flow transition, separation, and shockwave interference on the left wing during re-entry, resulting in a drastic increase in local temperature and ultimately the loss of control and destruction of the vehicle. Similar localized shell erosion also contributed to the failure of the US Falcon HTV-2 inaugural flight test, attributed one of the reasons to the "blind spots in understanding hypersonic boundary layer transition" [3].

Predicting transition is a significant fundamental scientific issue facing hypersonic vehicles, receiving high attention globally [3]. The US Hypersonic Research Program NHFRP (2010-2030) lists boundary layer transition as a major focus, stating: "The performance of supersonic combustion ramjet engines and the prediction of boundary layer transition are the two most critical technical areas. For the enhancement of future design capabilities and increased confidence, these two technological areas are of equal importance". In addition to theoretical research and ground experiments, dedicated flight tests specifically targeting transition are flourishing [1], such as the US-Australian joint HIFire-1 and HIFire-5 tests, the US X-43A test, and numerous tests conducted in China.

The transition process strongly depends on the incoming flow and wall conditions [3] and involves multiple physical mechanisms. In high-altitude flows, the transition begins with the destabilization of laminar flows, encompassing four stages: receptivity (disturbance generation), linear stability (linear evolution of disturbances), nonlinear evolution of disturbances, and turbulence. Typical hypersonic vehicle flow instabilities include leading-edge instability (attachment-line mode), streamwise instability (1^{st} and 2^{nd} Mack modes, etc.), centrifugal instability (e.g., Görtler mode), crossflow instability (crossflow mode), and shear-layer instability (roughness elements, steps, etc.).

The flow transition process during trans-atmospheric flight is highly coupled with high-temperature gas effects. The dramatic increase in heat flux caused by flow transition accelerates high-temperature gas reactions and wall ablation and catalysis. However, the mechanisms by which high-temperature gas effects and wall effects influence the transition process remain unclear: on one hand, high-temperature gas effects lead to changes in the laminar boundary layer (reduced temperature and boundary layer thickness), triggering Mack mode disturbances and promoting transition; on the other hand, if thermochemical non-equilibrium processes absorb disturbance energy, transition is delayed, and vice versa.

This paper presents the authors' progress in the study of flow instabilities in hypersonic trans-atmospheric flight [4-8]. It encapsulates several significant findings, as follows: 1) Elucidation of the excitation mechanisms governing the evolution of the three-dimensional boundary layer at the vehicle nose, with particular emphasis on the impact of thermal–chemical nonequilibrium effects. 2) Observation of a notable decay in disturbance growth-rate oscillation downstream of the turning point, where the unstable supersonic mode transitions back to the subsonic regime. 3) Discovery of novel modes of crossflow vortices occurring on the surface of swept wings.

2. Governing equations

In hypersonic trans-atmospheric flight, the flow temperature increases considerably behind shocks and towards the wall, where the vibrational energy and chemical dissociation become significant. A good approximation considered is the five-species model of air (N_2, O_2, NO, N, O). Additional conservation equations of species mass and vibrational energy are needed as compared with CPG flows. The two-temperature model of Park [2] is adopted, which includes a translational/rotational temperature T and a vibrational temperature T_v. The resulting Navier–Stokes equations for the TCNE flow take the following forms.

(i) Continuity equation:

$$\frac{\partial \rho}{\partial t} + \nabla \cdot (\rho \boldsymbol{u}) = 0 \tag{2.2a}$$

(ii) Momentum equation:

$$\frac{\partial \rho}{\partial t} + \nabla \cdot (\rho \boldsymbol{u}) = -\nabla p + \nabla \cdot \boldsymbol{\tau} \tag{2.2b}$$

(iii) Energy equation:

$$\frac{\partial \rho E}{\partial t} + \nabla \cdot (\rho H \boldsymbol{u}) = \nabla \cdot \left(\boldsymbol{u} \cdot \boldsymbol{\tau} - \boldsymbol{q}_{tr} + \boldsymbol{q}_v - \sum_{m=1}^{5} h_m \boldsymbol{d}_m \right) \tag{2.2c}$$

(iv) Species continuity equation (species index $s \in [2, 5]$):

$$\frac{\partial \rho_s}{\partial t} + \nabla \cdot (\rho_s \boldsymbol{u}) = -\nabla \boldsymbol{d}_s + \dot{\omega}_s \tag{2.2d}$$

(v) Vibrational energy equation:

$$\frac{\partial \rho e_v}{\partial t} + \nabla \cdot (\rho e_v \boldsymbol{u}) = -\nabla \left(\boldsymbol{q}_v + \sum_{m=1}^{3} e_{v,m} + \boldsymbol{d}_m \right) + Q_{t-v} \tag{2.2e}$$

(vi) Equation of state:

$$p = \rho R T = \rho T \sum_{m=1}^{5} R_m Y_m \tag{2.2f}$$

Here ρ and p are the density and pressure; $\boldsymbol{u} = [u, v, w]^{\mathrm{T}}$ is the velocity vector; $c_{p,t-r}$ and $c_{vib} = \partial e_v / \partial T_v$ are the translational–rotational and vibrational components of specific heat, respectively, where e_v denotes the specific vibrational energy; the species mass fraction $Y_s = \rho_s / \rho$ and R_s is the species gas constant; h_s denotes the species specific enthalpy; and the species vibrational energy is calculated using the characteristic vibrational temperature [9].

The mixture's viscosity μ and thermal conductivity $k_{t-r}$and k_v are calculated through the relations from Gupta et al. [10], which are as accurate as the solution of the first-order Chapman–Enskog approximation in the absence of ions [11]. The molecular collision integrals required in the relations are evaluated from the curve fits of Capitelli et al. [12]. The mass diffusion coefficient ρDsm is associated with μ through a constant Schmidt number $S_c = 0.5$. Miró et al. [9,13] concluded that the use of different mass-diffusion models or a moderate variation of S_c had small influences on the boundary layer instabilities. The source terms Q_{t-v} and $\dot{\omega}_s$ describe the finite-rate energy relaxation and chemical reactions, respectively. The energy relaxation between transitional and vibrational components is modelled using the Landau–Teller equation [14].

Five chemical reactions among the five species are considered here:

$$\left.\begin{array}{lrcl} R_1: & N_2 + M & \leftrightarrow & 2N + M \\ R_2: & O_2 + M & \leftrightarrow & 2O + M \\ R_3: & NO + M & \leftrightarrow & N + O + M \\ R_4: & N_2 + O & \leftrightarrow & NO + N \\ R_5: & NO + O & \leftrightarrow & O_2 + N \end{array}\right\} \tag{2.3}$$

where M is a third body. The chemical equilibrium constants are calculated based on the species Gibbs free energy fitted by McBride, Zehe & Gordon [15]. The forward reaction constants are from the relations of Park, Jaffe & Partridge [16].

The ten basic variables of $\mathrm{Eq.}(2.2)$ are $\boldsymbol{q} = [\rho, u, v, w, T, Y_s, T_v]$ with $s \in [2,5]$. Hence $\mathrm{Eq.}(2.2)$ is expressed in an operator form as

$$\mathrm{N}(\boldsymbol{q}) = \boldsymbol{S}(\boldsymbol{q}) \tag{2.4}$$

where the operator N includes unsteady, convection and diffusion terms, while $\boldsymbol{S}$ denotes the TCNE source term related to $\dot{\omega}_s$ and Q_{t-v}. The combination of ρ and four Y_s, rather than five ρ_s, is selected as the basic variables here because once $\boldsymbol{S}$ is set to $\boldsymbol{0}$, Y_s and T_v are constants throughout the flow field under homogeneous boundary conditions, then $\mathrm{Eq.}(2.2)$ reduces to the same form as that for CPG flows: $\mathrm{N}(\boldsymbol{q}) = \boldsymbol{0}$.

3. Numerical methods

3.1. Laminar flow solver

A steady laminar flow is required prior to stability analyses. In this work, Eq.(2.2) is solved in Cartesian coordinates through a fifth-order shock-fitting solver [17]. Two implicit time-marching schemes are utilized for efficiency increase, including GMRES (generalized minimal residual) and line relaxation methods. As the swept body is of infinite span, the flow is assumed to be uniform in the spanwise direction. The boundary conditions at the wall are no-slip, isothermal or adiabatic, and non-catalytic, i.e. $(\partial Y_s/\partial\eta)_w = 0$. In the far field, the boundary is located at the shock, and the post-shock parameters are obtained from the Rankine–Hugoniot relation. A symmetry condition is imposed at the boundary of $s = 0$. A non-reflecting boundary condition is adopted for the outflow boundary based on characteristic variables.

Sufficient grid points of 401 are used in the wall-normal direction to ensure grid independence (see supplementary material available at https://doi.org/10.1017/jfm.2022.607 for details). In the streamwise direction, the grid density required for a converged laminar flow is lower than that for NPSE calculations, so it is determined by the latter. At most, around 40 points are distributed within one streamwise wavelength of disturbance mode.

3.2. Linear instability theory and parabolized stability analysis

Here LST and PSE are used to efficiently calculate the linear and nonlinear growth of the cross-flow disturbance. Their frameworks are briefly described below as widely used techniques [18]. The variable $\bar{\boldsymbol{q}}$ is decomposed into a steady laminar part $\bar{\boldsymbol{q}}$ and a disturbed part $\tilde{\boldsymbol{q}}$.Here $\bar{\boldsymbol{q}} = [\bar{\rho}, \bar{U}, \bar{V}, \bar{W}, \bar{T}, \bar{Y}_s, T_v]$is the laminar flow solution, and $\tilde{\boldsymbol{q}} = [\tilde{\rho}, \tilde{u}, \tilde{v}, \tilde{w}, \tilde{T}, \tilde{Y}_s, \tilde{T}_v]$ is the disturbance. The disturbance governing equation is written as

$$\mathrm{N}\,(\bar{\boldsymbol{q}} + \tilde{\boldsymbol{q}}) - \mathrm{N}\,(\bar{\boldsymbol{q}}) = \boldsymbol{S}(\bar{\boldsymbol{q}} + \tilde{\boldsymbol{q}}) - \boldsymbol{S}(\bar{\boldsymbol{q}}) \tag{3.1}$$

The expanded matrix form of Eq.(3.1) in the$(s - \eta - z)$coordinates is

$$\begin{aligned} \boldsymbol{F}\frac{\partial\tilde{\boldsymbol{q}}}{\partial t} + \frac{\boldsymbol{A}}{h_1}\frac{\partial\tilde{\boldsymbol{q}}}{\partial s} + \boldsymbol{B}\frac{\partial\tilde{\boldsymbol{q}}}{\partial\eta} + \boldsymbol{C}\frac{\partial\tilde{\boldsymbol{q}}}{\partial z} + \boldsymbol{D}\tilde{q} = \frac{\boldsymbol{H}_{ss}}{h_1^2}\frac{\partial^2\tilde{\boldsymbol{q}}}{\partial s^2} + \boldsymbol{H}_{\eta\eta}\frac{\partial^2\tilde{\boldsymbol{q}}}{\partial\eta^2} \\ + \boldsymbol{H}_{zz}\frac{\partial^2\tilde{\boldsymbol{q}}}{\partial z^2} + \frac{\boldsymbol{H}_{s\eta}}{h_1}\frac{\partial^2\tilde{\boldsymbol{q}}}{\partial s\partial\eta} + \frac{\boldsymbol{H}_{sz}}{h_1}\frac{\partial^2\tilde{\boldsymbol{q}}}{\partial s\partial z} + H_{\eta z}\frac{\partial^2\tilde{\boldsymbol{q}}}{\partial\eta\partial z} + \boldsymbol{N} \end{aligned} \tag{3.2}$$

Here$h_1 = 1 + \kappa_0\eta$ is the Lamé coefficient related to the streamwise curvature κ_0; matrices$\boldsymbol{F}, \boldsymbol{A}, \boldsymbol{B}, \boldsymbol{C}, \boldsymbol{D}$ and $\boldsymbol{H}$ are all 10 × 10 matrices just dependent on $\bar{\boldsymbol{q}}$; and $\boldsymbol{N}$ represents the nonlinear term. The expressions of these matrix coefficients are very elaborate, especially in TCNE flows, and the software MAPLE is thus employed to ensure correctness. The following Fourier decomposition of a disturbance is introduced:

$$\tilde{\boldsymbol{q}}(s,\eta,z,t) = \sum_{m=-\boldsymbol{M}_{max}}^{\boldsymbol{M}_{max}} \sum_{n=-\boldsymbol{N}_{max}}^{N_{max}} \hat{\boldsymbol{q}}_{mn}(s,\eta)\exp\left[i\left(\int_{s_0}^{s}\alpha_{mn}(s)ds + n\beta z - m\omega t\right)\right] \tag{3.3}$$

where $M_{\max}$ and $N_{\max}$ represent one-half of the number of modes kept in the truncated Fourier series; s_0 is the computational onset; ω and β are the specified circular frequency and spanwise wavenumber, respectively; $\alpha_{mn} = \alpha_{mn,r} + i\alpha_{mn,i}$is the complex streamwise wavenumber; and $\hat{\boldsymbol{q}}_{\mathrm{mn}}$ stands for the shape function. A phase velocity is defined as $c_{mn,r} = m\omega/\left[\alpha_{mn,r}^2 + (n\beta)^2\right]^{1/2}$. For brevity, a notation (m,n) is introduced for the mode with a circular frequency of $m\omega$ and a spanwise wavenumber of $n\beta$. Mode $(0,0)$ is also called mean flow distortion, as a modification to the laminar flow after temporal and spanwise average.

The PSE for each mode takes the following form:

$$\hat{\boldsymbol{A}}_{mn}\frac{\partial\hat{\boldsymbol{q}}_{mn}}{\partial s} = -\left(\hat{\boldsymbol{D}}_{mn}\hat{\boldsymbol{q}}_{mn} + \hat{\boldsymbol{B}}_{mn}\frac{\partial\hat{\boldsymbol{q}}_{mn}}{\partial\eta} + \hat{\boldsymbol{C}}_{mn}\frac{\partial^2\hat{\boldsymbol{q}}_{mn}}{\partial\eta^2}\right) + \hat{\boldsymbol{N}}_{mn}\exp\left(-i\int_{s_0}^{s}\alpha_{mn}ds\right) \tag{3.4}$$

where the matrix coefficients are functions of $\alpha_{mn}, m\omega, n\beta$ and the matrices in Eq.(3.2), and $\hat{\boldsymbol{N}}_{\mathrm{mn}}$ is the Fourier component of $\boldsymbol{N}$ and acts as a nonlinear forcing term. For LST, the nonlinear term is neglected and the flow is further assumed to be locally parallel, i.e. $\partial/\partial s = 0$. Hence the base wall-normal velocity is also assumed zero from the continuity equation. As a result, an eigenvalue problem is established for

each Fourier mode [19]. For PSE analysis, Eq.(3.4) is solved through a streamwise marching procedure. The auxiliary condition adopted to determine α_{mn} is based on the disturbance kinetic energy. The wall-normal discretization uses the Chebyshev collocation point method and the streamwise one uses the Euler scheme. In addition, a relaxation factor is introduced to improve numerical robustness at large amplitudes of harmonic waves [20].

The disturbance boundary conditions at the wall are consistent with those for laminar flow:

$$\text{At } \eta = 0: \hat{u}_{mn} = \hat{v}_{mn} = \hat{w}_{mn} = \frac{\partial \hat{Y}_{s,mn}}{\partial \eta} = 0, \begin{cases} \hat{T}_{mn} = \hat{T}_{v,mn} = 0, & \text{if isothermal} \\ \dfrac{\partial \hat{T}_{mn}}{\partial \eta} = \dfrac{\partial \hat{T}_{v,mn}}{\partial \eta} = 0, & \text{if adiabatic} \end{cases} \tag{3.5}$$

The $\hat{\rho}_{mm}$ at the wall is solved through the disturbed continuity equation. For the boundary conditions at the shock, the disturbed Rankine–Hugoniot relation is solved to account for the shock–disturbance interaction [21].

The present PSE solver for TCNE flows has been verified with the DNS data in the authors' previous works [5,6]. Comparisons with the existing results of cross-flow instability cases are provided in the supplementary material.

3.3. Secondary instability analysis

Large-amplitude cross-flow vortices are subject to various types of high-frequency instabilities. The SIT can be used to obtain the disturbance characteristics by solving the instability equation on the distorted base flow. For stationary cross-flow vortices, the NPSE solution is written as

$$\tilde{\boldsymbol{q}}_{NPSE}(s,\eta,z) = \sum_{n} A_{0n}\hat{\boldsymbol{q}}_{0n} \exp\left[in\left(\int_{s_0}^{s} \alpha_r ds + \beta z\right)\right] \tag{3.6}$$

where A_{0n} is the mode's amplitude and α_r stands for the real part of the fundamental wavenumber. Therefore, the distorted base flow is $\bar{\boldsymbol{q}}' = \bar{\boldsymbol{q}} + \tilde{\boldsymbol{q}}_{NPSE}$, and the secondary instability disturbance to be solved is $\tilde{\boldsymbol{q}}_{\mathrm{sd}}$. The exponent in Eq.(3.6) depends on two coordinates, so a coordinate transformation is introduced to make the exponent one-coordinate-dependent. The wave front $z_r = z_r(s_r)$ is

$$z_r = \int_{s_0}^{s_r} tan\,\theta_2 ds + z_0\,, \qquad tan\,\theta_2 = -\frac{\alpha_r}{\beta} \tag{3.7a,b}$$

where θ_2 is the slope angle and z_0 is a reference point. Physically, the tangent line indicates the direction of the cross-flow vortex axis, and thus a local vortex-oriented coordinate $(s_2 - \eta_2 - z_2)$, with its origin at $(s = s_r, \eta = 0, z = z_r)$, can then be defined as

$$\left.\begin{aligned} s_2 &= (z - z_r)\sin\theta_2 + (s - s_r)\cos\theta_2 \\ z_2 &= (z - z_r)\cos\theta_2 - (s - s_r)\sin\theta_2 \\ \eta_2 &= \eta \end{aligned}\right\} \tag{3.8}$$

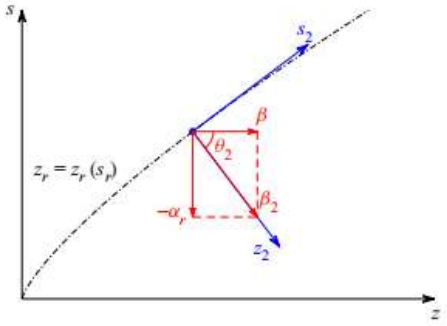

Figure 1. Definition of the vortex-oriented coordinates.

A schematic of this vortex-oriented coordinate is provided in Figure 1. A locally parallel flow is further assumed in SIT, such that at a given location $s = s_r$, the s-derivatives of $A_{0n}\hat{\boldsymbol{q}}_{0n}$ are much smaller than the η-derivatives, so the s-dependence of A_{0n}, α_r and $\hat{\boldsymbol{q}}_{0n}$ is neglected in a small region near s_r [22,

23]. This is reasonable because strong secondary instability usually occurs where the cross-flow vortices are saturated. Consequently, the disturbance in Eq.(3.6) near $s = s_r$ is rewritten as

$$\tilde{\boldsymbol{q}}_{\text{NPSE}}(\eta_2, z_2) = \sum_n A_{0n}\hat{\boldsymbol{q}}_{0n}(\eta_2)\exp(in\beta_2 z_2) \tag{3.9}$$

where $\beta_2 = \beta/cos\ \theta_2$ is the z_2-direction wavenumber. As a result of the locally-parallel-flow assumption, $\tilde{\boldsymbol{q}}_{\text{NPSE}}$ is explicitly independent of s_2 and periodic in the z_2 direction.

The velocities in the vortex-oriented coordinates are

$$u_2 = w\sin\theta_2 + u\cos\theta_2\,, \qquad w_2 = w\cos\theta_2 - u\sin\theta_2\,, \qquad v_2 = v \tag{3.10a-c}$$

Therefore, the variable in SIT is $\boldsymbol{q_2} = [\rho, u_2, v_2, w_2, T, Y_s, T_v]$, and the base flow distorted by the stationary cross-flow vortex is

$$\bar{\boldsymbol{q}}_2'(\eta_2, z_2) = \bar{\boldsymbol{q}}(\eta_2) + \sum_n A_{0n}\hat{\boldsymbol{q}}_{2,0n}(\eta_2)\exp(in\beta_2 z_2) \tag{3.11}$$

Similarly, the disturbance to be solved is replaced as $\tilde{\boldsymbol{q}}_{2,\text{sd}}$, and the governing equation is

$$\text{N}\left(\bar{\boldsymbol{q}}_2' + \tilde{\boldsymbol{q}}_{2,sd}\right) - \text{N}\left(\bar{\boldsymbol{q}}_2'\right) = S\left(\bar{\boldsymbol{q}}_2' + \tilde{\boldsymbol{q}}_{2,sd}\right) - \boldsymbol{S}(\bar{\boldsymbol{q}}_2') \tag{3.12}$$

which can be expanded into a similar form to Eq. (3.2)

Equation (3.12) is solved through the Floquet theory [18], so a temporal-mode solution is written as

$$\tilde{\boldsymbol{q}}_{2,sd} = \varepsilon\left\{\sum_{n=-N_{sd}}^{N_{sd}} \hat{\boldsymbol{q}}_{2,n}(\eta_2)\exp[i(n+\sigma_d)\beta_2 z_2]\right\}\exp(\omega_s t + i\alpha_s s_2) \tag{3.13}$$

where ε is the mode amplitude, $\omega_s = \omega_{s,r} + i\omega_{s,i}$ the temporal characteristic exponent, $\omega_{s,r}$ the mode growth rate and $\omega_{s,i}$ the shift in the circular frequency. Also, σ_d denotes the detuning parameter and N_{sd} is the truncated orders. The corresponding phase velocity is defined as $c_{s,r} = -\omega_{s,i}/\alpha_s$. After substituting Eqs. (3.11) and (3.13) into Eq. (3.12) and neglecting $O(\varepsilon^2)$ terms, a complex eigenvalue problem is obtained:

$$\mathcal{A}\hat{Q} = \omega_s\ \mathcal{B}\,\hat{Q} \tag{3.14}$$

Here $\hat{\boldsymbol{Q}}$ is the global eigenvector containing all $\hat{\boldsymbol{q}}_{2,\text{n}}$. Matrices $\mathcal{A}$ and $\mathcal{B}$ are global matrices with dimensions of $\left[10\text{N}_\text{y} \times (2\text{N}_\text{sd}+1)\right]^2$. The boundary conditions for $\hat{\boldsymbol{q}}_{2,n}$ at the wall are

$$\text{At}\ \eta = 0\text{:}\ \ \hat{u}_{2,n} = \hat{v}_{2,n} = \hat{w}_{2,n} = \hat{T}_n = \hat{T}_{v,n} = \hat{Y}_{s,n} = 0 \tag{3.15}$$

The main consideration is that the frequency of the secondary cross-flow instability mode is usually high (of the order of 100KHz), so $\hat{T}_n, \hat{T}_{v,n}$ and $\hat{Y}_{s,n}$ are forced to vanish at the wall owing to the thermal inertia of the solid body [19, 24]. The Dirichlet conditions in Eq.(3.15) are also used at the far-field boundary because $\hat{\boldsymbol{q}}_{2,n}$ quickly decays outside the boundary layer. The eigenvalues and eigenvectors of the large-scale matrices are solved through the same algorithm as that in LST. More details can be found in Koch et al. [25] and Ren & Fu [26].

4. Results and discussion

4.1 Mach 20 flows past a 7 deg blunt cone

Table 1. Free-stream conditions for the Mach 20 flow over a blunt cone

M_∞	$p_\infty(Pa)$	$T_\infty(K)$	$U_\infty(m/s)$	$\text{Re}_\infty\ (/m)$	$Y_{N_2,\infty}$	$T_w(K)$
20	2549.2	221.55	5967.7	1.686×10^7	0.767	1000

The test case is based on a blunt cone with a nose radius of 3 mm and a half angle of 7°. The free-stream conditions correspond to the altitude of 25 km, as listed in Table 1. The wall temperature of

1000 K is set over most of the cone surface. In the nose sphere region, however, a radiative wall-boundary condition is employed to allow higher wall temperature due to high local heat flow.

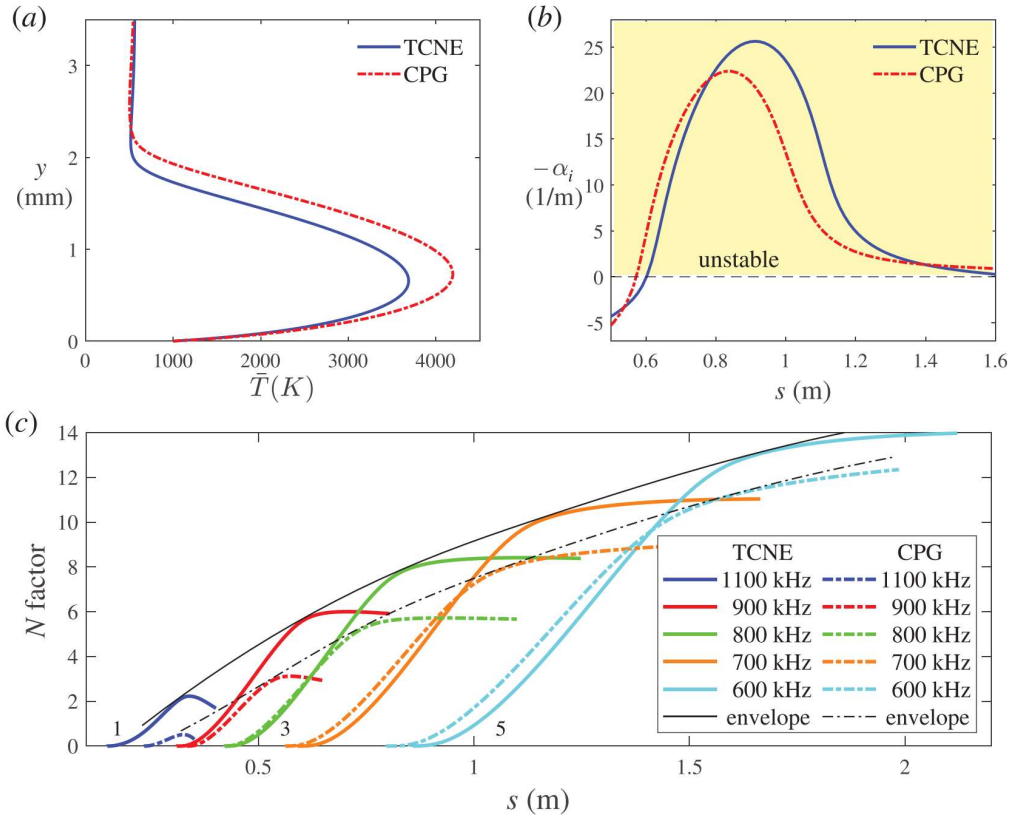

Fig. 2 Comparisons of (a) the laminar flow profile, (b) the growth rate curves with an f value of 700 kHz, and (c) the N factor curves

In the linear case as shown in Fig. 2, the second mode is destabilized and its frequency increases as the boundary layerbecomes cooler and thinner. Therefore, the maximum growth ratein the TCNE case is 15% higher and the peak location shifts downstream. The differences between the maximum N factors at thesefrequencies range from 1.5 to 2.8. As a result, the envelop of the N factors in the TCNE flow moves upstream in the regime from 0.13m to 0.34 m.

Figure 3 shows the comparisons between the CPG and TCNE results of the secondary growth rates in the fundamental resonance. Three sets of curves are shown with different A2nd values. With the increasing amplitude, the TCNE effects increase both the maximum secondary growth rate and the corresponding azimuthal wavenumber.

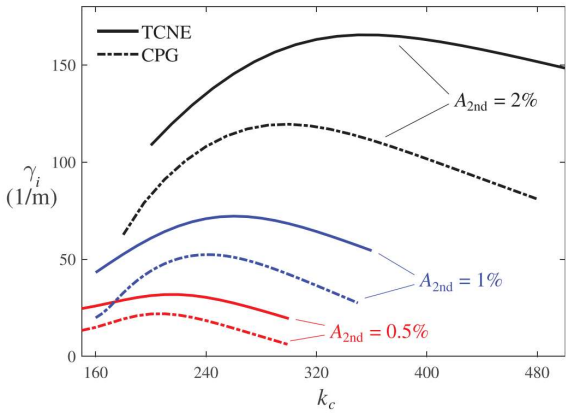

Fig. 3 Secondary growth rates for the CPG and TCNE cases in the fundamental resonance

Particularly, Figure 4 depicts the **supersonic mode** instabilities, as found by the present authors, in thermal–chemical nonequilibrium [6]. Spontaneous radiation of sound is observed in both cases because of the existence of the synchronization. The pressure disturbances of two cases oscillate outside the boundary layer at supersonic phase speed. When the disturbance returns into the subsonic region downstream, it decays outside the boundary layer, except for the beam of sound waves from upstream.

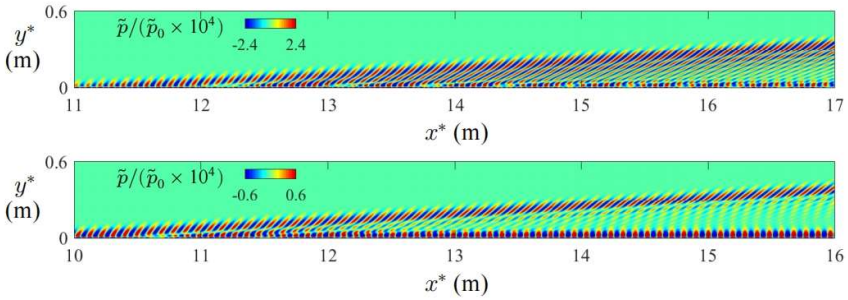

Fig. 4 Instantaneous pressure disturbance of different wall temperature for the Mach 20 TCNE flow case.

4.2 Mach 16 flow over a swept parabola

The three-dimensional boundary layer over a swept wing of infinite span is considered herein. The swept wing is modelled by a swept parabolic body, which was widely adopted in previous investigations concerning cross-flow instability [7, 27, 28]. The geometry is described as

$$y^2 = 2r_0 x \quad \text{and} \quad r_0 = 0.01m \tag{4.1a, b}$$

Where r_0 is the radius of curvature at the leading edge. A schematic of the geometry and computational domain is provided in Figure 5, where x, y and z are the Cartesian coordinates with the spanwise z direction along the stagnation line. The sweep angle Λ results in a non-zero spanwise velocity $W_\infty = Q_\infty \sin \Lambda$ at zero angles of attack, where Q_∞ is the free-stream velocity. In terms of stability analyses, a local body-fitted coordinate (s–η–z) is defined as sketched, where s denotes the streamwise direction along the surface with its origin at the stagnation line and η is the wall-normal coordinate.

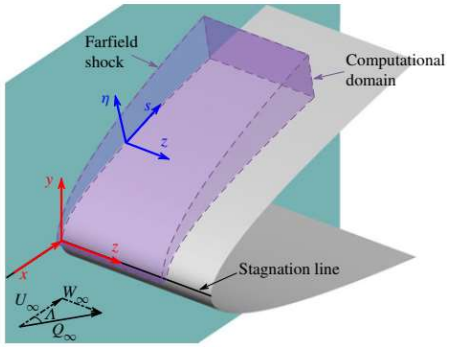

Fig. 5. Schematic of the geometry and computational domain, as well as the coordinate systems. Here x, y and z are the Cartesian coordinates, and s, η and z are the local body-fitted coordinates.

Table 2. Flow conditions of Mach-16 flow over a swept parabola.

Ma_∞	$\Lambda(deg.)$	$Re_\infty(m^{-1})$	$T_\infty(K)$	$p_\infty(Pa)$	$Q_\infty(ms^{-1})$	$Y_{N_2,\infty}$	$T_w(K)$
16	45	8.404×10^6	224.5	1616	4806	0.767	1500

The flow conditions of the benchmark case are listed in Table 2, where the subscript ∞ denotes free-stream values, and T_w is the wall temperature. The free-stream conditions correspond to an altitude of 28 km.

The laminar flow field is investigated first. The flow is also calculated under the CPG assumption for comparison to clarify the effect of TCNE. Instead of Sutherland's law, the same air composition and transport models as described in § 2 are adopted for consistency. Figure 6(*a*) provides the laminar temperature contours in the TCNE and CPG benchmark cases around the nose region of the parabola. A noticeable difference is that the temperature in the TCNE case is much lower than that in the CPG case due to strong thermochemical processes downstream of the shock. The difference is most obvious downstream of the normal shock at $y = 0$, and the distributions of $\bar{T}$ and $\bar{T}_v$ along the streamline at $y = 0$ are plotted in figure 6(*b*). In the CPG case, $\bar{T}$ slowly increases downstream until a sudden drop at $x > -0.23$ mm due to the specified low *Tw*. In comparison, $\bar{T}$ in the TCNE case quickly decreases downstream of the shock, and is at most 2268 K lower than that of the CPG case. As a result, the shock stand-off distance is 32% smaller at $y = 0$. The decrease of temperature in the TCNE case is accompanied by the rise of the vibrational energy and mass fractions of *NO*, *O* and *N*. Vibrational temperature $\bar{T}_v$ rapidly increases to over 4500 K and tends to vibrational equilibrium further downstream towards the wall. Moreover, large fractions of *NO* and *O* are produced, as shown in figure 6(*c*), and the minimum mass fractions of N_2 and O_2 are 0.737 and 0.114, respectively.

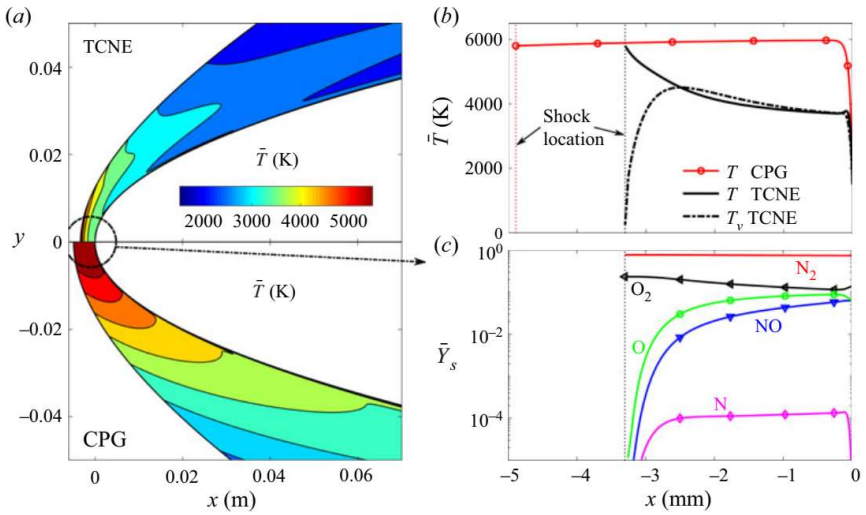

Fig 6. (a) Laminar temperature contours around the nose region, and the streamwise distribution of (b) temperatures and (c) species mass fractions (TCNE only) along the streamline at y = 0 in the TCNE and CPG benchmark cases.

Eq.(3.13) is used to reproduce the three-dimensional (s_2–η_2–z_2) distribution of $\tilde{u}_{2,sd}$, which is applicable under the locally-parallel-flow assumption. Figure 7 illustrates the spatial structures of $\tilde{u}_{2,sd}$ of the four modes near $s = 0.90$ m. The temporal sequence (t–η_2–z_2) of $\tilde{u}_{2,sd}$ at a fixed s_2 exhibits the same structures except in the opposite (-t) direction. Alternating inclined strips are observed for $\tilde{u}_{2,sd}$ of the type-I mode, which is quite similar to those documented in the low-speed experiments through a proper orthogonal decomposition [29]. Also, the streamwise wavelength ($2\pi/\alpha_s$) of the type-I mode is severaltimes larger than that of the other three modes. For the type-II1 mode, inclined curved strips are observed on the top of the vortex. Their orientation is consistent with the base-flow streamlines. In comparison, the two type-IV modes exhibit aligned-arrow and inclined-dumbbell shapes in the downwash region of the vortex.

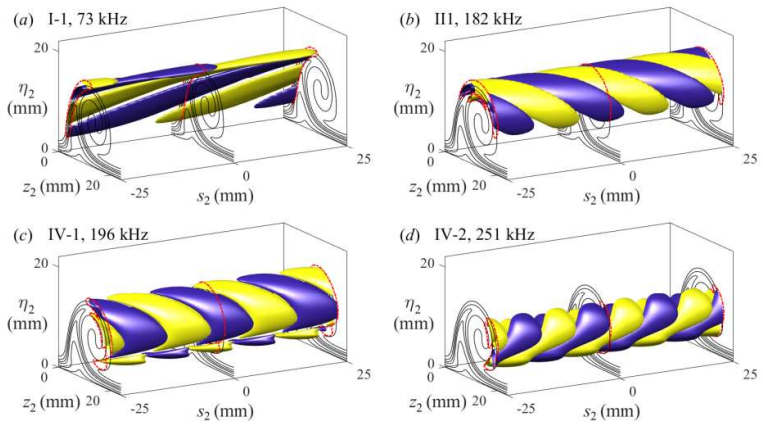

Fig 7. Isosurfaces of the normalized streamwise velocity (Re$(\tilde{u}_{2,sd})$/ max $|\tilde{u}_{2,sd}|$ = ±0.2) for the modes near s = 0.9 m: (*a*) type-I-1, (*b*) type-II1, (*c*) type-IV-1 and (*d*) type-IV-2 modes. The black solid lines are the contours of the base streamwise velocity and the red dash-dotted lines the contours of $|\tilde{u}_{2,sd}|$/ max $|\tilde{u}_{2,sd}|$ at 0.2.

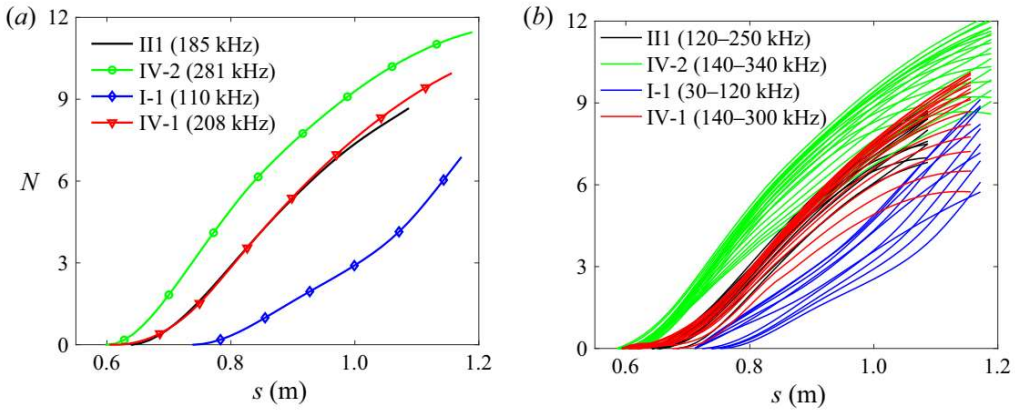

Fig 8. Streamwise distribution of the N factors for the four secondary instability modes in the TCNE benchmark case (*a*) at the frequencies related to their local maximum growth rates and (*b*) within specific frequency bands with Δf = 10 kHz

Next, we focus on the accumulative growth (N factors) of these secondary instability modes in the streamwise direction to find the spatially dominant one. There are generally two approaches to obtain the spatial growth rate. The first is to solve the spatial-mode version of Eq.(3.13), i.e. solve for the complex α_s at a given real ω_s. The second is to use the extended Gaster transformation, where the temporal growth rate is transformed to a spatial one through a group velocity. Comparisons show that the growth rate differences of the type-I-1, type-II1 and type-IV modes by these two methods are less than 2 % at s = 1.0 m, so the extended Gaster transformation also works in this high-enthalpy flow. Nevertheless, small differences exist so the spatial-mode calculation is performed in the following to obtain the disturbance N factors. Figure 8 gives the N factor distribution of the four modes at the frequencies related to their maximum growth rates. The N factor envelopes within specific frequency bands are also plotted. The type-IV-2 mode is observed to have the largest N factor with the onset at s = 0.59 m. The N factors of the type-IV-1 and type-II1 modes are close to each other, and the N factor of the type-I-1 mode is the lowest within the computational domain. In short, the present results highlight the vital role of the type-IV modes. This is the first report, to the authors' knowledge, wherein a secondary instability mode, located at the downwash region of the stationary cross-flow vortex, has the largest N factor in hypersonic boundary layers.

5. Conclusion

In this study, we have developed a linear Parabolized Stability Equation (PSE) solver tailored for Thermal–Chemical Nonequilibrium (TCNE) flows. Specifically, we investigated the impact of TCNE on disturbance evolution and structures in Mach 20 flows around a 7-degree blunt cone, with a particular focus on the behavior of the supersonic mode. Our analysis revealed that the primary resonance governs secondary instability, with stationary structures prevailing over fundamental waves. Additionally, our examination of Mach 16 flows over a swept parabola underscored the crucial role of type-IV modes in the secondary instability region, particularly highlighting the significance of the type-IV-2 mode, which exhibits the highest N factor in hypersonic boundary layers.

While the constraints of space preclude an exhaustive discussion, it is noteworthy that our study did not delve into the characteristics of attachment-line instability and the predominant modes downstream. Nevertheless, these findings contribute significantly to our understanding of the intricate dynamics of hypersonic flows under thermal–chemical nonequilibrium conditions. Moreover, they offer valuable insights into the factors influencing flow stability and transition within such environments.

Acknowlegements

Support from the National Key Research and Development Plan of China through project No. 2019YFA0405200, the National Key Project (Grant No. GJXM92579), NSFC grant 12202242 and 12172195, Yancheng MetaStone Co. is gratefully acknowledged.

References

1. Candler G V. Rate effects in hypersonic flows. Annual Review of Fluid Mechanics, 2019; 51: 379-402.
2. Anderson J D. Hypersonic and high-temperature gas dynamics. Second Edition. McGraw-Hill, 2006.
3. Fu S, Wang L. RANS modeling of high-speed aerodynamic flow transition with consideration of stability theory. Progress in Aerospace Sciences, 2013; 58: 36-59.
4. Chen X, Wang L, Fu S. Energy transfer of hypersonic and high--enthalpy boundary layer instabilities and transition. Physical Review Fluids, 2022, 7(3), 033901
5. Chen XL, Wang L, Fu S. Secondary instability of the hypersonic high-enthalpy boundary layers with thermal-chemical nonequilibrium effects. Physics of Fluids, 2021, 33(3): 34132.
6. Chen XL, Wang L, Fu S. Parabolized Stability Analysis of Hypersonic Thermal-Chemical Nonequilibrium Boundary-Layer Flows. AIAA Journal, 2021, 59(7): 2382-2395.
7. Xi YC, Wang L, Fu S, Ren J. Receptivity and stability of hypersonic leading-edge sweep flows around a blunt body. Journal of Fluid Mechanics, R2; PII S0022112021002172
8. Xi YC, Wang L, Fu S, Ren J. Cross-flow vortices and their secondary instabilities in hypersonic and high-enthalpy boundary layers. Journal of Fluid Mechanics, 2022.
9. MIRÓ MIRÓ, F., PINNA, F., BEYAK, E.S., BARBANTE, P. & REED, H.L. 2018 Diffusion and chemical non-equilibrium effects on hypersonic boundary-layer stability. In 2018 Aerospace Sciences Meeting. AIAA Paper 2018-1824.
10. GUPTA, R.N., YOS, J.M. & THOMPSON, R.A. 1990 A review of reaction rates and thermodynamic and transport properties for the 11-species air model for chemical and thermal nonequilibrium calculations to 30000 K. NASA RP-1232.
11. BOTTIN, B., ABEELE, D.V., MAGIN, T.E. & RINI, P. 2006 Transport properties of collision-dominated dilute perfect gas mixtures at low pressures and high temperatures. Prog. Aerosp. Sci. 42 (1), 38–83.

12. CAPITELLI, M., GORSE, C., LONGO, S. & GIORDANO, D. 2000 Collision integrals of high-temperature air species. J. Thermophys. Heat Transfer 14 (2), 259–268.
13. MIRÓ MIRÓ, F., BEYAK, E.S., PINNA, F. & REED, H.L. 2019 High-enthalpy models for boundary-layer stability and transition. Phys. Fluids 31 (4), 044101.
14. PARK, C. 1990 Nonequilibrium Hypersonic Aerothermodynamics. John Wiley & Sons
15. MCBRIDE, B.J., ZEHE, M.J. & GORDON, S. 2002 NASA Glenn coefficients for calculating thermodynamic properties of individual species. NASA/TP-2002-211556.
16. PARK, C., JAFFE, R.L. & PARTRIDGE, H. 2001 Chemical-kinetic parameters of hyperbolic Earth entry.J. Thermophys. Heat Transfer 15 (1), 76–90.
17. CHEN, X. & FU, S. 2020 Convergence acceleration for high-order shock-fitting methods in hypersonic flow applications with efficient implicit time-stepping schemes. Comput. Fluids 210, 104668.
18. HERBERT, T. 1997 Parabolized stability equations. Annu. Rev. Fluid Mech. 29, 245–283.
19. MALIK, M.R. 1990 Numerical methods for hypersonic boundary layer stability. J. Comput. Phys. 86 (2),376–413.
20. ZHAO, L., ZHANG, C., LIU, J. & LUO, J. 2016 Improved algorithm for solving nonlinear parabolized stability equations. Chin. Phys. B 25 (8), 238–245.
21. CHANG, C.-L., VINH, H. & MALIK, M.R. 1997 Hypersonic boundary-layer stability with chemical reactions using PSE. In 28th Fluid Dynamics Conference. AIAA Paper 1997-2012.
22. KOCH, W., BERTOLOTTI, F.P., STOLTE, A. & HEIN, S. 2000 Nonlinear equilibrium solutions in a three-dimensional boundary layer and their secondary instability. J. Fluid Mech. 406, 131–174.
23. BONFIGLI, G. & KLOKER, M. 2007 Secondary instability of crossflow vortices: validation of the stability theory by direct numerical simulation. J. Fluid Mech. 583, 229–272.
24. BITTER, N.P. & SHEPHERD, J.E. 2015 Stability of highly cooled hypervelocity boundary-layers. J. Fluid Mech. 778, 586–620.
25. KOCH, W., BERTOLOTTI, F.P., STOLTE, A. & HEIN, S. 2000 Nonlinear equilibrium solutions in athree-dimensional boundary layer and their secondary instability. J. Fluid Mech. 406, 131–174.
26. REN, J. & FU, S. 2015 Secondary instabilities of Görtler vortices in high-speed boundary layer flows. J. Fluid Mech. 781, 388–421.
27. MACK, C.J. & SCHMID, P.J. 2010 Direct numerical study of hypersonic flow about a swept parabolic body.Comput. Fluids 39 (10), 1932–1943.
28. XU, G., CHEN, J., LIU, G., DONG, S. & FU, S. 2019 The secondary instabilities of stationary cross-flow vortices in a Mach 6 swept wing flow. J. Fluid Mech. 873, 914–941.
29. GROOT, K.J., SERPIERI, J., PINNA, F. & KOTSONIS, M. 2018 Secondary crossflow instability through global analysis of measured base flows. J. Fluid Mech. 846, 605–653.